CMES, vol.15, no.1, pp.49-67, 2006

Wavelet Based 2-D Spectral Finite Element Formulation for Wave Propagation Analysis in Isotropic Plates

Mira Mitra and S. Gopalakrishnan[1]

Abstract: In this paper, a 2-D Wavelet based Spectral Finite Element (WSFE) is developed and is used to study wave propagation in an isotropic plate. Here, first, wavelet approximation is done in both temporal and one spatial (lateral) dimension to reduce the governing partial differential wave equations to a set of Ordinary Differential Equations (ODEs). Daubechies compactly supported orthogonal scaling functions are used as basis which allows finite domain analysis and easy imposition of initial/boundary conditions. However, the assignment of initial and boundary conditions in time and space respectively, are done following two different methods. Next, the reduced ODEs are solved exactly to derive the shape functions which are used to form the elemental dynamic stiffness matrix. Similar to the conventional Fast Fourier Transform (FFT) based Spectral Finite Element (FSFE) method which has problems in handling finite boundaries, the present method also reduces the computational cost substantially compared to conventional Finite Element (FE) method. The proposed method can also be used directly for both time and frequency domain analysis like FSFE. However, importantly, the use of localized basis functions in 2-D WSFE method circumvents several serious limitations of the corresponding 2-D FSFE technique. The formulated 2-D WSFE is used to study axial and transverse wave propagations in isotropic plates of different configurations. The simulated responses are also validated with 2-D FE results.

keyword: Wave propagation; Wavelets; Spectral finite element; Isotropic plates

1 Introduction

Study of elastic wave propagation is important to understand the behavior of the structure under high frequency impact loadings such as gust, tool drop, bird hit, etc. In addition, it is becoming more relevant recently for applications like structural health monitoring using diagnostic waves, control of noise and vibration, etc.

Numerical solution of wave equations requires high accuracy in numerical differentiation and at the same time has larger spatial grids and time steps to make it computationally efficient. FE modeling is not suited for this purpose primarily because wave propagation problems deal with excitations of high frequency content. In FE modeling, the element size should be comparable to wavelength which is very small at high frequencies. This results in large system size and enormous computational cost. Thus, in general, alternative numerical techniques [Andreaus, Batra, and Porfiri (2005), Han, Ding, and Liu (2005), Qian, Han, Ufimtsev, and Atluri (2004)] are adopted for such analysis. Spectral Finite Element Method (SFEM) popularized by Doyle (1999) is one such numerical method, especially tailored for wave propagation analysis. In short, SFEM follows FE modeling procedure in the transformed frequency domain.

2-D FSFE for isotropic materials was formulated [Rizzi (1989), Rizzi and Doyle (1989), Rizzi and Doyle (1991)] following the same procedures as in 1-D case. Here, nodal displacements are related to nodal tractions through frequency-wavenumber dependent stiffness matrix. Similar to 1-D case, mass distribution is captured exactly and the accurate elemental dynamic stiffness matrix is derived. Consequently, in absence of any discontinuities, one element is sufficient to model a plate structure of any length, but unbounded along the other lateral direction. Later recently, 2-D FSFE was formulated for anisotropic [Chakraborty and Gopalakrishnan (2004b)] and inhomogeneous [Chakraborty and Gopalakrishnan (2004c)] materials, for in-plane motions. Here, instead of a-priori Helmhöltz decomposition of displacement fields, the partial wave technique [Solie and Auld (1973)] was adopted. The method was further extended to model anisotropic plates under both in-plane and out-of-plane loadings [Chakraborty and Gopalakrishnan (2005)].

[1] Department of Aerospace Engineering, Indian Institute of Science, Bangalore 560 012. INDIA, e-mail: krishnan@aero.iisc.ernet.in, Fax: +91-80-2360-0134

The main drawback of FSFE is that it cannot handle waveguides of short lengths. This is because, the required assumption of periodicity in time approximation results in "wrap around" problem for smaller time window, which totally distorts the response. However, the 1-D WSFE [Mitra and Gopalakrishnan (2005)] developed using Daubechies compactly supported wavelets [Daubechis (1992)] with localized basis removes the "wrap around" problem and can efficiently model undamped finite length waveguides. In addition, for 2-D problems, FSFE [Doyle (1999)] are essentially semi-infinite i.e they are bounded only in one direction. Thus, the effect of one lateral boundary cannot be captured and this can be attributed to the global basis functions of the Fourier series approximation of the spatial dimension. The 2-D WSFE presented here, also overcomes the above problem and can accurately model 2-D plate structures of finite dimensions. This is again due to the use of localized Daubechies scaling functions as basis for approximation of the spatial dimension.

The steps followed in 2-D WSFE formulation are quite similar to those for 2-D FSFE. Here, first Daubechies scaling functions are used for approximation in time and this reduces the governing Partial Differential Equation (PDE) into a set of coupled PDEs in spatial dimensions. Wavelet extrapolation technique [Williams and Amaratunga (1997)] is used for adapting wavelet in finite domain and imposition of initial conditions. The coupled transformed PDEs are decoupled through eigen analysis. Though the eigen analysis involved is time consuming, this can be computed and stored as it is not dependent on the particular problem. Next, each of these decoupled PDEs are further reduced to a set of coupled ODEs by using the same Daubechies scaling functions for approximation of the spatial dimension. Unlike the temporal approximation, here, the scaling function coefficients lying outside the finite domain are not extrapolated but obtained through periodic extension for unrestrained i.e free lateral edges. However, other boundary conditions, e.g fixed-fixed, free-fixed etc, are imposed through a restraint matrix [Patton and Marks (1996), Chen, Hwang, and Shih (1996)]. Each set of ODEs are also coupled, but here, decoupling can only be done for unrestrained boundary conditions i.e free-free. These are explained in detail in the later part of the paper.

It should be mentioned here that similar to 2-D FSFE, the frequency dependent wave characteristics corresponding to each lateral (Y) wavenumber, can be extracted directly from the present 2-D WSFE formulation. However, unlike FSFE, the wavenumbers will be accurate only up to a certain fraction of Nyquist frequency [Mitra and Gopalakrishnan (2006)].

The paper is organized as follows. In Section 2, a brief overview of the orthogonal bases of Daubechies compactly supported wavelets are presented. In Section 3, the governing differential equations are derived. In the following two sections, the details of 2-D WSFE formulation is given for isotropic plates. In Section 6, various numerical results are presented for both in-plane and out-of-plane wave propagation in plates of different configurations. The responses simulated with 2-D WSFE are validated with 2-D FE results. Here, the advantages of using 2-D WSFE over 2-D FSFE are also explained through numerical examples. The paper end with some important conclusions.

2 Daubechies Compactly Supported Wavelets

In this section, a concise review of orthogonal basis of Daubechies wavelets [Daubechis (1992)] is provided. Wavelets, $\psi_{j,k}(t)$ forms compactly supported orthonormal basis for $\mathbf{L^2}(\mathbf{R})$. The wavelets and associated scaling functions $\varphi_{j,k}(t)$ are obtained by translation and dilation of single functions $\psi(t)$ and $\varphi(t)$ respectively.

$$\psi_{j,k}(t) = 2^{j/2}\psi(2^j t - k), \qquad j,k \in \mathbf{Z} \tag{1}$$

$$\varphi_{j,k}(t) = 2^{j/2}\varphi(2^j t - k), \qquad j,k \in \mathbf{Z} \tag{2}$$

The scaling functions $\varphi(t)$ are derived from the dilation or scaling equation,

$$\varphi(t) = \sum_k a_k \varphi(2t - k) \tag{3}$$

and the wavelet function $\psi(t)$ is obtained as

$$\psi(t) = \sum_k (-1)^k a_{1-k}\varphi(2t - k) \tag{4}$$

a_k are the filter coefficients and they are fixed for specific wavelet or scaling function basis. For compactly supported wavelets only a finite number of a_k are nonzero.

The filter coefficients a_k are derived by imposing certain constraints on the scaling functions which are as follows. (1) The area under scaling function is normalized to one.

$$\int_{-\infty}^{\infty} \varphi(t)dt = 1 \tag{5}$$

(2) The scaling function $\varphi(t)$ and its translates are orthonormal

$$\int_{-\infty}^{\infty} \varphi(t)\varphi(t+k)dt = \delta_{0,k} \qquad k \in \mathbf{Z} \tag{6}$$

and (3) wavelet function $\psi(t)$ has M vanishing moments

$$\int_{-\infty}^{\infty} \psi(t)t^m dt = 0 \qquad m = 0,\ldots,M \tag{7}$$

The number of vanishing moments M denotes the order N of the Daubechies wavelet, where $N = 2M$.

Let $P_j(f)(t)$ be the approximation of a function $f(t)$ in $\mathbf{L^2}(\mathbf{R})$ using $\varphi_{j,k}(t)$ as basis, at a certain level (resolution) j, then

$$P_j(f)(t) = \sum_k c_{j,k}\varphi_{j,k}(t), \qquad k \in \mathbf{Z} \tag{8}$$

where, $c_{j,k}$ are the approximation coefficients. Let $Q_j(f)(t)$ be the approximation of the function using $\psi_{j,k}(t)$ as basis, at the same level j.

$$Q_j(f)(t) = \sum_k d_{j,k}\psi_{j,k}(t), \qquad k \in \mathbf{Z} \tag{9}$$

where, $d_{j,k}$ are the detail coefficients. The approximation $P_{j+1}(f)(t)$ to the next finer level of resolution $j+1$ is given by

$$P_{j+1}(f)(t) = P_j(f)(t) + Q_j(f)(t) \tag{10}$$

This forms the basis of multi resolution analysis associated with wavelet approximation.

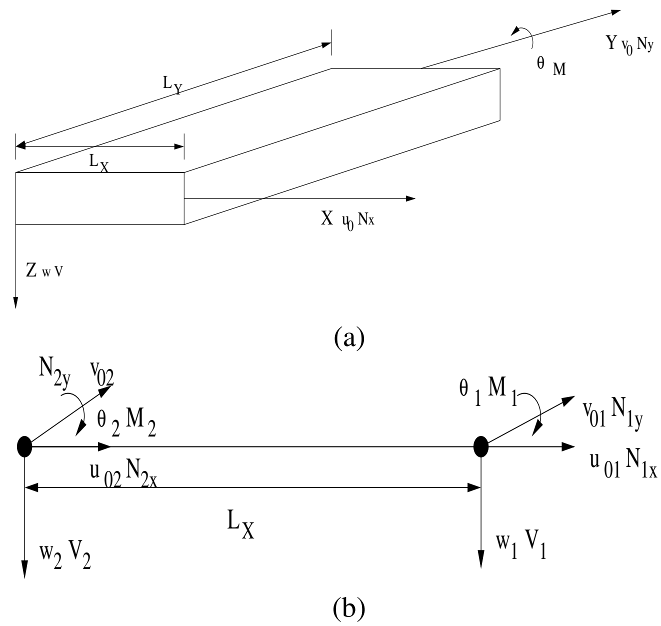

Figure 1 : (a) Plate element and (b) nodal forces and displacements.

3 Governing Differential Equations

The displacement fields, according to Classical Plate Theory (CPT) [Nayfeh and Pai (2004)] are

$$u(x,y,z,t) = u_0(x,y,t) - z\partial w/\partial x \tag{11}$$

$$v(x,y,z,t) = v_0(x,y,t) - z\partial w/\partial y \tag{12}$$

$$w(x,y,z,t) = w(x,y,t) \tag{13}$$

where, $u_0(x,y,t)$, $v_0(x,y,t)$ and $w(x,y,t)$ are the axial and transverse displacements respectively along the mid-plane (see Fig. 1(a)). The mid-plane of the plate is at $z = 0$. The associated non-zero strains are obtained as

$$\begin{Bmatrix} \varepsilon_{xx} \\ \varepsilon_{yy} \\ \varepsilon_{xy} \end{Bmatrix} = \begin{Bmatrix} \partial u_0/\partial x \\ \partial v_0/\partial y \\ \partial u_0/\partial y + \partial v_0/\partial x \end{Bmatrix} + \begin{Bmatrix} -\partial^2 w/\partial x^2 \\ -\partial^2 w/\partial y^2 \\ -2\partial^2 w/\partial x\partial y \end{Bmatrix} = \{\varepsilon_0\} + \{\varepsilon_1\} \tag{14}$$

Here, ε_{xx} and ε_{yy} are the normal strains in x and y direction respectively, while, ε_{xy} is the in-plane shear strain. The constitutive relation for isotropic materials are given as

$$\begin{Bmatrix} \sigma_{xx} \\ \sigma_{yy} \\ \sigma_{xy} \end{Bmatrix} = \begin{bmatrix} Q_{11} & Q_{12} & 0 \\ Q_{12} & Q_{22} & 0 \\ 0 & 0 & Q_{66} \end{bmatrix} \begin{Bmatrix} \varepsilon_{xx} \\ \varepsilon_{yy} \\ \varepsilon_{xy} \end{Bmatrix} \tag{15}$$

where, σ_{xx} and σ_{yy} are the normal stresses in x and y directions respectively and σ_{xy} is the in-plane shear stress. The expressions for Q_{ij} in terms of Young's modulus E and Poisson's ratio ν are given in reference Nayfeh and Pai (2004). The force resultants are defined in terms of these stresses as

$$\left\{\begin{array}{c} N_{xx} \\ N_{yy} \\ N_{xy} \end{array}\right\} = \int_A \left\{\begin{array}{c} \sigma_{xx} \\ \sigma_{yy} \\ \sigma_{xy} \end{array}\right\} dA,$$
$$\left\{\begin{array}{c} M_{xx} \\ M_{yy} \\ M_{xy} \end{array}\right\} = \int_A z \left\{\begin{array}{c} \sigma_{xx} \\ \sigma_{yy} \\ \sigma_{xy} \end{array}\right\} dA, \tag{16}$$

where, the integration is performed over the cross-sectional area A. Substituting Eqns. 15 and 14 in Eqn. 16, and considering symmetric cross-section, the relation between the force resultants and displacement fields are obtained as

$$\left\{\begin{array}{c} N_{xx} \\ N_{yy} \\ N_{xy} \end{array}\right\} = \left[\begin{array}{ccc} A_{11} & A_{12} & 0 \\ A_{12} & A_{22} & 0 \\ 0 & 0 & A_{66} \end{array}\right] \{\varepsilon_0\},$$
$$\left\{\begin{array}{c} M_{xx} \\ M_{yy} \\ M_{xy} \end{array}\right\} = \left[\begin{array}{ccc} D_{11} & D_{12} & 0 \\ D_{12} & D_{22} & 0 \\ 0 & 0 & D_{66} \end{array}\right] \{\varepsilon_1\} \tag{17}$$

The stiffness coefficients A_{ij} and D_{ij} are defined as

$$[A_{ij},\, D_{ij}] = \int_A Q_{ij}[1,\, z^2] dA$$

Similarly, the inertial coefficients used in later part of the section are defined as

$$[I_0,\, I_2] = \int_A \rho[1,\, z^2] dA$$

where, ρ is the mass density. Total strain Π and kinetic energies T are calculated as

$$\Pi = \frac{1}{2}\int_0^L \int_A (\sigma_{xx}\varepsilon_{xx} + \sigma_{yy}\varepsilon_{yy} + \sigma_{xy}\varepsilon_{xy}) dx dA \tag{18}$$

$$T = \frac{1}{2}\int_0^L \int_A \rho(\dot{u}^2 + \dot{v}^2 + \dot{w}^2) dx dA \tag{19}$$

Using Hamilton's principle, the minimization of the above energies with respect to the three degrees of freedom $(u_0,\ v_0,\ w)$ will give three differential equations which can be written in terms of the resultant forces and moments as

$$\partial N_{xx}/\partial x + \partial N_{xy}/\partial y = I_0 \ddot{u}_0 \tag{20}$$

$$\partial N_{xy}/\partial x + \partial N_{yy}/\partial y = I_0 \ddot{v}_0 \tag{21}$$

$$\begin{aligned} &\partial^2 M_{xx}/\partial x^2 + 2\partial^2 M_{xy}/\partial x\partial y + \partial^2 M_{yy}/\partial y^2 \\ &\quad = I_0\ddot{w} - I_2(\partial^2\ddot{w}/\partial x^2 + \partial^2\ddot{w}/\partial y^2) \end{aligned} \tag{22}$$

The governing differential equations can be written in terms of displacements by substituting Eqns. 14 and 17 in Eqns. 20 to 22 as

$$\begin{aligned} &A_{11}\partial^2 u_0/\partial x^2 + (A_{12}+A_{66})\partial^2 v_0/\partial x\partial y \\ &\quad + A_{66}\partial^2 v_0/\partial y^2 = I_0\ddot{u}_0 \end{aligned} \tag{23}$$

$$\begin{aligned} &A_{66}\partial^2 v_0/\partial x^2 + (A_{12}+A_{66})\partial^2 u_0/\partial x\partial y \\ &\quad + A_{22}\partial^2 v_0/\partial y^2 = I_0\ddot{v}_0 \end{aligned} \tag{24}$$

$$\begin{aligned} &D_{11}\partial^4 w/\partial x^4 + 2(D_{12}+2D_{66})\partial^4 w/\partial x^2\partial y^2 \\ &\quad + D_{22}\partial^4 w/\partial y^4 = -I_0\ddot{w} \\ &\quad + I_2(\partial^2\ddot{w}/\partial x^2 + \partial^2\ddot{w}/\partial y^2) \end{aligned} \tag{25}$$

The associated boundary conditions are

$$N_x = N_{xx}n_x + N_{xy}n_y, \quad N_y = N_{xy}n_x + N_{yy}n_y \tag{26}$$

$$M_x = -M_{xx}n_x - M_{xy}n_y,$$

$$M_y = -M_{xy}n_x - M_{yy}n_y \tag{27}$$

$$\begin{aligned} Q = &(\partial M_{xx}/\partial x + \partial M_{xy}/\partial y + I_2\partial\ddot{w}/\partial x)n_x \\ &+ (\partial M_{xy}/\partial x + \partial M_{yy}/\partial y + I_2\partial\ddot{w}/\partial y)n_y \end{aligned} \tag{28}$$

where, N_x and N_y are the normal forces in x and y direction respectively. M_y and M_x are the moments about x and y axis and Q is the transverse shear force in z direction. For edges parallel to the y axis, $n_x = \pm 1$ and $n_y = 0$, thus for modeling a rectangular plate, the boundary conditions given by Eqns. 26 to 28 will contain only the terms associated with n_x. In addition, the shear resultant or the Kirchoff shear [Doyle (1999)], V is obtained as

$$V = Q - \partial M_{xy}/\partial y \tag{29}$$

This modification is done by considering M_{xy} as a couple caused by vertical forces at a small distance apart. This helps to reduce the number of boundary forces to four namely N_x, N_y, V and M_y as required by CPT. Using the

Eqn. 29, the boundary forces for edges parallel to y axis written in terms of displacements are of the form

$$N_x = A_{11}\partial u_0/\partial x + A_{12}\partial v_0/\partial y,$$

$$N_y = A_{66}(\partial u_0/\partial y + \partial v_0/\partial x) \tag{30}$$

$$M_y = D_{11}\partial^2 w/\partial x^2 + D_{12}\partial^2 w/\partial y^2 \tag{31}$$

$$V = -D_{11}\partial^3 w/\partial x^3 - D_{12}\partial^3 w/\partial x\partial y^2 + I_2\partial\ddot{w}/\partial x \tag{32}$$

In the following section, governing PDEs and the associated boundary conditions derived here are reduced to a set of ODEs using Daubechies scaling function approximation in time and one spatial (Y) dimension.

4 Reduction of Wave Equations to ODEs

4.1 Temporal Approximation

The first step of formulation of 2-D WSFE is the reduction of each of the three governing differential equations given by Eqns. 23 to 25 to a set of PDEs by Daubechies scaling function based transformation in time. The procedure is very similar to that done for formulating 1-D WSFE, where, the governing PDEs are reduced to sets of ODEs [Mitra and Gopalakrishnan (2005)]. However, it is described here in brief, for completeness. Let $u_0(x,y,t)$ be discretized at n points in the time window $[0\ t_f]$. Let $\tau = 0,\ 1,\dots,\ n-1$ be the sampling points, then

$$t = \triangle t\tau \tag{33}$$

where, $\triangle t$ is the time interval between two sampling points. The function $u_0(x,y,t)$ can be approximated by scaling function $\varphi(\tau)$ at an arbitrary scale as

$$u_0(x,y,t) = u_0(x,y,\tau) = \sum_k u_{0k}(x,y)\varphi(\tau-k), \quad k\in\mathbf{Z} \tag{34}$$

where, $u_{0k}(x,y)$ (referred as u_{0k} hereafter) are the approximation coefficient at a certain spatial dimension x and y. The other displacements $v_0(x,y,t)$, $w(x,y,t)$ can be transformed similarly and Eqn. 23 can be written as

$$\sum_k\left(A_{11}\frac{\partial^2 u_{0k}}{\partial x^2} + (A_{12}+A_{66})\frac{\partial^2 v_{0k}}{\partial x\partial y} + A_{66}\frac{\partial^2 u_{0k}}{\partial y^2}\right)\varphi(\tau-k) = \frac{I_0}{\triangle t^2}\sum_k u_k\varphi''(\tau-k) \tag{35}$$

Taking inner product on both sides of Eqns. 35 with the translates of scaling functions $\varphi(\tau-j)$, where $j = 0,\ 1,\dots,n-1$ and using their orthogonal properties, we get n simultaneous PDEs as,

$$A_{11}\frac{\partial^2 u_{0j}}{\partial x^2} + (A_{12}+A_{66})\frac{\partial^2 v_{0j}}{\partial x\partial y} + A_{66}\frac{\partial^2 u_{0j}}{\partial y^2} = \frac{1}{\triangle t^2}\sum_{k=j-N+2}^{j+N-2}\Omega^2_{j-k}I_0u_{0k} \quad j=0,\ 1,\dots,n-1 \tag{36}$$

where, N is the order of the Daubechies wavelet and Ω^2_{j-k} are the connection coefficients defined as

$$\Omega^2_{j-k} = \int\varphi''(\tau-k)\varphi(\tau-j)d\tau \tag{37}$$

Similarly, for first order derivative Ω^1_{j-k} are defined as

$$\Omega^1_{j-k} = \int\varphi'(\tau-k)\varphi(\tau-j)d\tau \tag{38}$$

For compactly supported wavelets, Ω^1_{j-k}, Ω^2_{j-k} are nonzero only in the interval $k = j-N+2$ to $k = j+N-2$. The details for evaluation of connection coefficients for different orders of derivative is given by Beylkin (1992). It can be observed from the PDEs given by Eqn. 36 that certain coefficients u_{0j} near the vicinity of the boundaries ($j=0$ and $j=n-1$) lie outside the time window $[0\,t_f]$ defined by $j=0,\ 1,\dots,n-1$. These coefficients must be treated properly for finite domain analysis. Here, a wavelet based extrapolation scheme [Williams and Amaratunga (1997)] is implemented for solution of boundary value problems. This approach allows treatment of finite length data and uses polynomial to extrapolate the coefficients lying outside the finite domain either from interior coefficients or initial/boundary values. The method is particularly suitable for approximation in time for the ease to impose initial values. The above method converts the PDEs given by Eqns 36 to a set of coupled PDEs given as

$$A_{11}\left\{\frac{\partial^2 u_{0j}}{\partial x^2}\right\} + (A_{12}+A_{66})\left\{\frac{\partial^2 v_{0j}}{\partial x\partial y}\right\} + A_{66}\left\{\frac{\partial^2 u_{0j}}{\partial y^2}\right\} = [\Gamma^1]^2 I_0\{u_{0j}\} \tag{39}$$

where Γ^1 is the first order connection coefficient matrix obtained after using the wavelet extrapolation technique. It should be mentioned here that though the connection coefficients matrix, Γ^2, for second order derivative can be obtained independently, here it is written as

$[\Gamma^1]^2$ as it helps to impose the initial conditions [Mitra and Gopalakrishnan (2005)]. These coupled PDEs are decoupled using eigenvalue analysis

$$\Gamma^1 = \Phi\Pi\Phi^{-1} \tag{40}$$

where, Π is the diagonal eigenvalue matrix and Φ is the eigenvectors matrix of Γ^1. Let the eigenvalues be $\imath\gamma_j$, $\imath = \sqrt{-1}$, then the decoupled ODEs corresponding to Eqns. 39 are

$$A_{11}\frac{\partial^2 \widehat{u}_{0j}}{\partial x^2} + (A_{12}+A_{66})\frac{\partial^2 \widehat{v}_{0j}}{\partial x \partial y} + A_{66}\frac{\partial^2 \widehat{u}_{0j}}{\partial y^2} = -I_0\gamma_j^2\widehat{u}_{0j} \quad j=0,\ 1,\ldots,n-1 \tag{41}$$

where, $\widehat{u}_{0j}$ and similarly other transformed displacements are

$$\widehat{u}_{0j} = \Phi^{-1}u_{0j} \tag{42}$$

Following exactly the similar steps, the final transformed form of the Eqns. 24 and 25 are

$$A_{66}\frac{\partial^2 \widehat{v}_{0j}}{\partial x^2} + (A_{12}+A_{66})\frac{\partial^2 \widehat{u}_{0j}}{\partial x \partial y} + A_{22}\frac{\partial^2 \widehat{v}_{0j}}{\partial y^2} = -I_0\gamma_j^2\widehat{v}_{0j} \tag{43}$$

$$D_{11}\frac{\partial^4 \widehat{w}_j}{\partial x^4} + 2(D_{12}+2D_{66})\frac{\partial^4 \widehat{w}_j}{\partial x^2 \partial y^2} + D_{22}\frac{\partial^4 \widehat{w}_j}{\partial y^4} = I_0\gamma_j^2\widehat{w}_j - I_2\gamma_j^2\left(\frac{\partial^2 \widehat{w}_j}{\partial x^2} + \frac{\partial^2 \widehat{w}_j}{\partial y^2}\right) \tag{44}$$

Similarly, the transformed form of the force boundary conditions given by Eqns. 30 to 32 are

$$A_{11}\frac{\partial \widehat{u}_{0j}}{\partial x} + A_{12}\frac{\partial \widehat{v}_{0j}}{\partial y} = \widehat{N}_{xj}$$

$$A_{66}\left(\frac{\partial \widehat{u}_{0j}}{\partial y} + \frac{\partial \widehat{v}_{0j}}{\partial x}\right) = \widehat{N}_{yj} \tag{45}$$

$$D_{11}\frac{\partial^2 \widehat{w}_j}{\partial x^2} + D_{12}\frac{\partial^2 \widehat{w}_j}{\partial y^2} = \widehat{M}_{yj} \tag{46}$$

$$-D_{11}\frac{\partial^3 \widehat{w}_j}{\partial x^3} - D_{12}\frac{\partial^3 \widehat{w}_j}{\partial x \partial y^2} - I_2\gamma_j^2\frac{\partial \widehat{w}_j}{\partial x} = \widehat{V}_j \quad j=0,\ 1,\ldots,n-1 \tag{47}$$

where, $\widehat{N}_{xj}$ and similarly $\widehat{N}_{yj}$, $\widehat{M}_{yj}$, $\widehat{V}_j$ are the transformed $N_x(x,y,t)$ and $N_y(x,y,t)$, $M_y(x,y,t)$, $V(x,y,t)$ respectively.

4.2 Spatial (Y) *Approximation*

As said earlier in Section 1, the next step involved is to further reduce each of the transformed and decoupled PDEs given by Eqns. 41, 43 and 44 for $j=0,\ 1,\ldots,n-1$ to a set of coupled ODEs using Daubechies scaling function approximation in one of the spatial (Y) direction. Similar to time approximation, the transformed variable $\widehat{u}_{0j}$ be discretized at m points in the spatial window $[0,\ L_Y]$, where L_Y is the length in Y direction. Let $\zeta = 0,\ 1,\ldots,\ m-1$ be the sampling points, then

$$y = \triangle Y\zeta \tag{48}$$

where, $\triangle Y$ is the spatial interval between two sampling points. The function $\widehat{u}_{0j}(x,y)$ can be approximated by scaling function $\varphi(\zeta)$ at an arbitrary scale as

$$\widehat{u}_{0j}(x,y) = \widehat{u}_{0j}(x,\zeta) = \sum_k \widehat{u}_{0lj}(x)\varphi(\zeta-l), \qquad l \in \mathbf{Z} \tag{49}$$

where, $\widehat{u}_{0lj}(x,y)$ (referred as $\widehat{u}_{0lj}$ hereafter) are the approximation coefficient at a certain spatial dimension x. The other displacements $\widehat{v}_{0j}(x,y)$, $\widehat{w}(x,y)$ can be transformed similarly and Eqn. 41 can be written as

$$\begin{aligned} &A_{11}\sum_l \frac{d^2\widehat{u}_{0lj}}{dx^2}\varphi(\zeta-l) \\ &+ (A_{12}+A_{66})\frac{1}{\triangle Y}\sum_l \frac{d\widehat{v}_{0lj}}{dx}\varphi'(\zeta-l) \\ &+ A_{66}\frac{1}{\triangle Y^2}\sum_l \widehat{u}_{0lj}\varphi''(\zeta-l) \\ &= -I_0\gamma_j^2\sum_l \widehat{u}_{0lj}\varphi(\zeta-l) \end{aligned} \tag{50}$$

Taking inner product on both sides of Eqn. 50 with the translates of scaling functions $\varphi(\zeta-i)$, where $i = 0,\ 1,\ldots,m-1$ and using their orthogonal properties, we get m simultaneous ODEs as,

$$\begin{aligned} &A_{11}\frac{d^2\widehat{u}_{0ij}}{dx^2} + (A_{12}+A_{66})\frac{1}{\triangle Y}\sum_{l=i-N+2}^{i+N-2}\frac{d\widehat{v}_{0lj}}{dx}\Omega^1_{i-l} \\ &+ A_{66}\frac{1}{\triangle Y^2}\sum_{l=i-N+2}^{i+N-2}\widehat{u}_{0lj}\Omega^2_{i-l} = -I_0\gamma_j^2\widehat{u}_{0ij} \\ &i=0,\ 1,\ldots,m-1 \end{aligned} \tag{51}$$

where, N is the order of Daubechies wavelet, Ω^1_{i-l} and Ω^2_{i-l} are the connection coefficients for first and second order derivative defined in Eqns. 38 and 37 respectively.

It can be seen from the ODEs given by Eqn. 51, that, similar to time approximation, here also certain coefficients $\widehat{u}_{0ij}$ near the vicinity of the boundaries ($i = 0$ and $i = m-1$) lie outside the spatial window $[0\ L_Y]$ defined by $i = 0,\ 1, \ldots, m-1$. These coefficients must be treated properly for finite domain analysis. However here, unlike time approximation, these coefficients are obtained through periodic extension, but only for free lateral edges, while other boundary conditions are imposed quite differently using a restraint matrix [Patton and Marks (1996); Chen, Hwang, and Shih (1996)] and is discussed in detail in the later part of the section. The unrestrained i.e free-free boundary conditions may also be imposed in a similar way using restraint matrix but it has been seen from the numerical experiments that the use of periodic extension gives accurate results. In addition, it allows decoupling of the ODEs using eigenvalue analysis and thus reduces the computational cost. Here, after expressing the unknown coefficients lying outside the finite domain in terms of the inner coefficients considering periodic extension, the ODEs given by Eqn. 51 can be written as a matrix equation of the form

$$A_{11}\left\{\frac{d^2\widehat{u}_{0ij}}{dx^2}\right\}+(A_{12}+A_{66})[\Lambda^1]\left\{\frac{d\widehat{v}_{0ij}}{dx}\right\} +A_{66}[\Lambda^1]^2\left\{\widehat{u}_{0lj}\right\}=-I_0\gamma_j^2\left\{\widehat{u}_{0ij}\right\} \tag{52}$$

where, $[\Lambda^1]$ is the first order connection coefficient matrix obtained after periodic extension and it is of the form

$$[\Lambda^1] = \frac{1}{\triangle Y}\begin{bmatrix} \Omega_0^1 & \Omega_{-1}^1 & \ldots & \Omega_{-N+2}^1 & \ldots & \Omega_{N-2}^1 & \ldots & \Omega_1^1 \\ \Omega_1^1 & \Omega_0^1 & \ldots & \Omega_{-N+3}^1 & \ldots & 0 & \ldots & \Omega_2^1 \\ \vdots & \vdots & \ldots & \vdots & \ldots & \vdots & \ldots & \vdots \\ \Omega_{-1}^1 & \Omega_{-2}^1 & \ldots & 0 & \ldots & \Omega_{N-3}^1 & \ldots & \Omega_0^1 \end{bmatrix} \tag{53}$$

The coupled ODEs given by Eqn. 52 are decoupled using eigenvalue analysis similar to that done in time approximation as

$$\Lambda^1 = \Psi\Upsilon\Psi^{-1} \tag{54}$$

where, Υ is the diagonal eigenvalue matrix and Ψ is the eigenvectors matrix of Λ^1. It should be mentioned here that matrix Λ^1 has a circulant form and its eigen parameters are known analytically Davis (1963). Let the eigenvalues be $\imath\beta_i$, then the decoupled ODEs corresponding to Eqns. 52 are

$$A_{11}\frac{d^2\widetilde{u}_{0ij}}{dx^2}-\imath\beta_i(A_{12}+A_{66})\frac{d\widetilde{v}_{0ij}}{dx}-\beta_i^2A_{66}\widetilde{u}_{0lj} = -I_0\gamma_j^2\widetilde{u}_{0ij} \quad i=0,\ 1,\ldots,m-1 \tag{55}$$

where, $\widetilde{u}_{0j}$ and similarly other transformed displacements are

$$\widetilde{u}_{0j} = \Psi^{-1}\widehat{u}_{0j} \tag{56}$$

Following exactly the similar steps, the final transformed and decoupled form of the Eqns. 43 and 44 are

$$A_{66}\frac{d^2\widetilde{v}_{0ij}}{dx^2}-\imath\beta_i(A_{12}+A_{66})\frac{d\widetilde{u}_{0ij}}{dx}-\beta_i^2A_{22}\widetilde{v}_{0ij} = -I_0\gamma_j^2\widetilde{v}_{0ij} \tag{57}$$

$$D_{11}\frac{d^4\widetilde{w}_{ij}}{dx^4}-2\beta_i^2(D_{12}+2D_{66})\frac{d^2\widetilde{w}_{ij}}{dx^2}+\beta_i^4D_{22}\widetilde{w}_{ij} = I_0\gamma_j^2\widetilde{w}_{ij}-I_2\gamma_j^2\left(\frac{d^2\widetilde{w}_{ij}}{dx^2}-\beta_i^2\widetilde{w}_{ij}\right) \tag{58}$$

Similarly, the transformed form of the force boundary conditions given by Eqns. 45 to 47 are

$$A_{11}\frac{d\widetilde{u}_{0ij}}{dx}-\imath\beta_iA_{12}\widetilde{v}_{0ij} = \widetilde{N}_{xij}$$

$$A_{66}\left(-\imath\beta_i\widetilde{u}_{0ij}+\frac{d\widetilde{v}_{0ij}}{dx}\right) = \widetilde{N}_{yij} \tag{59}$$

$$D_{11}\frac{d^2\widetilde{w}_{ij}}{dx^2}-\beta_i^2D_{12}\widetilde{w}_{ij} = \widetilde{M}_{yij} \tag{60}$$

$$-D_{11}\frac{d^3\widetilde{w}_{ij}}{dx^3}+\imath\beta_i^2D_{12}\frac{d\widetilde{w}_{ij}}{dx}-I_2\gamma_j^2\frac{d\widetilde{w}_{ij}}{dx} = \widetilde{V}_{ij} \quad i=0,\ 1,\ldots,m-1 \tag{61}$$

The final transformed ODEs given by Eqns. 55, 57, 58 and the boundary conditions Eqns. 59 to 61 are used for 2-D WSFE following a procedure very similar to 2-D FSFE formulation [Chakraborty and Gopalakrishnan (2005)] and is explained in the next section.

Next, for imposition of other restrained boundary conditions along the lateral edges of plate structure, first, Eqn. 51 is written in a different form as

$$A_{11}\frac{d^2\widehat{u}_{0ij}}{dx^2}+(A_{12}+A_{66})\frac{1}{\triangle Y}\sum_{l=i-N+2}^{m-1}\frac{d\widehat{v}_{0lj}}{dx}\Omega^1_{i-l}$$
$$+A_{66}\frac{1}{\triangle Y^2}\sum_{l=i-N+2}^{m-1}\widehat{u}_{0lj}\Omega^2_{i-l}=-I_0\gamma_j^2\widehat{u}_{0ij}$$
$$i=0,\ 1,\ldots,m-1 \tag{62}$$

This is done by taking inner product on both sides of Eqn. 50 with the translates of scaling functions $\varphi(\zeta-i)$, where $i=0$ to $(m-1)-(N-2)$ instead of $i=0$ to $(m-1)$. Thus, the above Eqn. 62 can be written in a matrix form as

$$A_{11}\left\{\frac{d^2\widehat{u}_{0ij}}{dx^2}\right\}+(A_{12}+A_{66})[\Lambda^1_{\mathrm{R}}]\left\{\frac{d\widehat{v}_{0ij}}{dx}\right\}$$
$$+A_{66}[\Lambda^1_{\mathrm{R}}]^2\left\{\widehat{u}_{0lj}\right\}=-I_0\gamma_j^2\left\{\widehat{u}_{0ij}\right\} \tag{63}$$

where, $[\Lambda^1_{\mathrm{R}}]$ is a $(m+N-2)\times(m+N-2)$. Now, at the two lateral boundaries given by $y=0$ and $y=L_Y$, $\widehat{u}_{0j}(x,y)$ or $\widehat{u}_{0j}(x,\zeta)$ can be written in terms of the coefficients $\widehat{u}_{0ij}$ as

$$\widehat{u}_{0j}(x,0)=\sum_{l=-N+2}^{0}\widehat{u}_{0lj}\varphi(-l) \tag{64}$$

$$\widehat{u}_{0j}(x,L_Y)=\widehat{u}_{0j}(x,m-1)=\sum_{l=m-N+2}^{m-1}\widehat{u}_{0lj}\varphi(m-1-l) \tag{65}$$

From Eqns. 64 and 65, the coefficients $\widehat{u}_{0(-N+2)j}$ and $\widehat{u}_{0(m-1)j}$ are derived in terms of the other coefficients and a $(m+N-2)\times(m+N-2)$ restraint matrix $[R]$ can be formed which is used for transformation from unrestrained to restrained coefficients as

$$\{\widehat{u}_{0ij}\}_{restrained}=[R]\{\widehat{u}_{0ij}\}_{unrestrained} \tag{66}$$

when the boundary conditions are specified in terms of the displacements. Similarly for boundary conditions given in terms of their derivatives e.g slope, Eqn. 66 can be written as

$$\left\{\frac{d\widehat{u}_{0ij}}{dy}\right\}_{restrained}=[R]\left\{\frac{d\widehat{u}_{0ij}}{dy}\right\}_{unrestrained} \tag{67}$$

The restraint matrix $[R]$ is rank deficient and its order is equal to the number of boundary conditions specified. $[R]$ is formed by inserting two rows obtained from Eqn. 64 and 65 to a $(m+N-2)\times m$ identity matrix. Thus, after imposing the restraint, e.g for a fixed-fixed boundary condition given by $\widehat{u}_{0j}(x,0)=\widehat{v}_{0j}(x,0)=0$ and $\widehat{u}_{0j}(x,L_Y)=\widehat{v}_{0j}(x,L_Y)=0$, Eqn. 63 will be of the form

$$A_{11}\left\{\frac{d^2\widehat{u}_{0ij}}{dx^2}\right\}+(A_{12}+A_{66})[\Lambda^1_{\mathrm{R}}][R]\left\{\frac{d\widehat{v}_{0ij}}{dx}\right\}$$
$$+A_{66}[\Lambda^1_{\mathrm{R}}]^2[R]\left\{\widehat{u}_{0ij}\right\}=-I_0\gamma_j^2\left\{\widehat{u}_{0ij}\right\} \tag{68}$$

Similarly, the other equation corresponding to Eqn. 43 is

$$A_{66}\left\{\frac{d^2\widehat{v}_{0ij}}{dx^2}\right\}+(A_{12}+A_{66})[\Lambda^1_{\mathrm{R}}][R]\left\{\frac{d\widehat{u}_{0ij}}{dx}\right\}$$
$$+A_{22}[\Lambda^1_{\mathrm{R}}]^2[R]\left\{\widehat{v}_{0ij}\right\}=-I_0\gamma_j^2\left\{\widehat{v}_{0ij}\right\} \tag{69}$$

Again, for fixed-fixed boundary condition (out-of-plane loading), $\widehat{w}_j(x,0)=\partial\widehat{w}_j/\partial y(x,0)=0$ and $\widehat{w}_j(x,L_Y)=\partial\widehat{w}_j/\partial y(x,L_Y)=0$ and the final reduced ODEs obtained from Eqn. 44 is

$$D_{11}\left\{\frac{d^4\widehat{w}_{ij}}{dx^4}\right\}+2(D_{12}+2D_{66})[\Lambda^1_{\mathrm{R}}][R][\Lambda^1_{\mathrm{R}}][R]\left\{\frac{d^2\widehat{w}_{ij}}{dx^2}\right\}$$
$$+D_{22}[\Lambda^1_{\mathrm{R}}]^3[R][\Lambda^1_{\mathrm{R}}][R]\left\{\widehat{w}_{ij}\right\}=I_0\gamma_j^2\{\widehat{w}_{ij}\}$$
$$-I_2\gamma_j^2\left(\left\{\frac{d^2\widehat{w}_{ij}}{dx^2}\right\}+[\Lambda^1_{\mathrm{R}}][R][\Lambda^1_{\mathrm{R}}][R]\{\widehat{w}_{ij}\}\right) \tag{70}$$

As mentioned earlier, the matrices involved in Eqns. 68 to 70 are rank deficient by two and thus the first and last rows and columns are truncated to solve the equations that is required for the spectral finite element formulation discussed in the next section. The coefficients $\widehat{u}_{0(-N+2)j}$ and $\widehat{u}_{0(m-1)j}$ are then obtained from the other coefficients using Eqns. 64 and 65 respectively. The boundary conditions, Eqns. 45 to 47 after transformation and imposition of restraints are

$$A_{11}\left\{\frac{d\widehat{u}_{0ij}}{dx}\right\}+A_{12}[\Lambda^1_{\mathrm{R}}][R]\left\{\widehat{v}_{0ij}\right\}=\left\{\widehat{N}_{xij}\right\}$$

$$A_{66}\left([\Lambda^1_{\mathrm{R}}][R]\left\{\widehat{u}_{0ij}\right\}+\left\{\frac{d\widehat{v}_{0ij}}{dx}\right\}\right)=\left\{\widehat{N}_{yij}\right\} \tag{71}$$

$$D_{11}\left\{\frac{d^2\widehat{w}_{ij}}{dx^2}\right\}+D_{12}[\Lambda^1_{\mathrm{R}}][R][\Lambda^1_{\mathrm{R}}][R]\left\{\widehat{w}_{ij}\right\}$$
$$=\left\{\widehat{M}_{yij}\right\} \tag{72}$$

$$-D_{11}\left\{\frac{d^3\widehat{w}_{ij}}{dx^3}\right\}-D_{12}[\Lambda_R^1][R]\left\{\frac{d^3\widehat{w}_{ij}}{dx^2}\right\} -I_2\gamma_j^2\left\{\frac{d\widehat{w}_{ij}}{dx}\right\}=\left\{\widehat{V}_{ij}\right\} \tag{73}$$

5 Spectral Finite Element Formulation

The degrees of freedom associated with the element formulation is shown in Fig. 1(b). The element has four degrees of freedom per node, which are $\widetilde{u}_{0ij}$, $\widetilde{v}_{0ij}$, $\widetilde{w}_{ij}$ and $\partial\widetilde{w}_{ij}/\partial x$. From the previous sections, for unrestrained lateral edges we get a set of decoupled ODEs (Eqns. 55, 57 and 58) for isotopic plate using CPT, in a transformed wavelet domain. These equations are required to be solved for $\widetilde{u}_{0ij}$, $\widetilde{v}_{0ij}$ $\widetilde{w}_{0ij}$ and the actual solutions $u_0(x,y,t)$, $v_0(x,y,t)$, $w(x,y,t)$ are obtained using inverse wavelet transform twice for spatial Y dimension and time. For finite length data, the wavelet transform and its inverse can be obtained using a transformation matrix [Williams and Amaratunga (1994)]. Here, the spectral finite element technique is explained for the decoupled ODEs given by Eqns. 55, 57 and 58 for unrestrained i.e free lateral edges. However, for restrained boundary conditions the transformed ODEs given by Eqns. 68 to 70 are coupled and spectral finite element formulation for such cases follows similar steps, except that for each time discretization points j, $m-N\times m-N$ matrix ODE is solved instead of m decoupled ODEs.

It can be seen that the transformed decoupled ODEs have a form similar to that in FSFE [Doyle (1999)] and thus, WSFE can be formulated following the same method as for FSFE formulation. In this section, the subscripts j and i are dropped hereafter for simplified notations and all the following equations are valid for $j=0,\ 1,\ \ldots,\ n-1$ and $i=0,\ 1,\ \ldots,\ m-1$ for each j.

The exact interpolating functions for an element of length L_X, obtained by solving Eqns. 55, 57 and 58 respectively are

$$\{\widetilde{u}_0(x),\ \widetilde{v}_0(x),\ \widetilde{w}(x)\}^T=[\mathbf{R}][\Theta]\{\mathbf{a}\} \tag{74}$$

where, $[\Theta]$ is a diagonal matrix with the diagonal terms $[e^{-k_1x},\ e^{-k_1(L_X-x)},\ e^{-k_2x},\ e^{-k_2(L_X-x)},\ e^{-k_3x},\ e^{-k_3(L_X-x)},\ e^{-k_4x},\ e^{-k_4(L_X-x)}]$ and $[\mathbf{R}]$ is a 3×8 amplitude ratio matrix for each set of k_1, k_2, k_3 and k_4.

$$[\mathbf{R}]=\begin{bmatrix} R_{11} & \ldots\ \ldots & R_{18}\\ R_{21} & \ldots\ \ldots & R_{28}\\ R_{31} & \ldots\ \ldots & R_{38}\end{bmatrix} \tag{75}$$

k_1, k_2, k_3 and k_4 are obtained by substituting Eqn. 74 in Eqns 55, 57 and 58 and solving the characteristic equation. The characteristic equation is obtained by equating the determinant of the 3×3 companion matrix to zero. The corresponding $[\mathbf{R}]$ is obtained using singular value decomposition of the matrix. This method of determining wavenumbers and corresponding amplitude ratios was developed to formulate FSFE for graded beam with Poisson's contraction [Chakraborty and Gopalakrishnan (2004a)]. k_1, k_2, k_3 and k_4 corresponds to the three modes and as explained in reference Mitra and Gopalakrishnan (2006), these are the wavenumbers but only up to a certain fraction of Nyquist frequency.

Here, $\{\mathbf{a}\}=\{$A, B, C, D, E, F, G, H$\}$ are the unknown coefficients to be determined from transformed nodal displacements $\{\widetilde{\mathbf{u}}^{\mathbf{e}}\}$, where $\{\widetilde{\mathbf{u}}^{\mathbf{e}}\}=\{\widetilde{u}_{01}\ \widetilde{v}_{01}\ \widetilde{w}_1\ \partial\widetilde{w}_1/\partial x\ \widetilde{u}_{02}\ \widetilde{v}_{02}\ \widetilde{w}_2\ \partial\widetilde{w}_2/\partial x\}$ and $\widetilde{u}_{01}\equiv\widetilde{u}_0(0)$, $\widetilde{v}_{01}\equiv\widetilde{v}_0(0)$, $\widetilde{w}_1\equiv\widetilde{w}(0)$, $\partial\widetilde{w}_1/\partial x\equiv\partial\widetilde{w}(0)/\partial x$ and $\widetilde{u}_{02}\equiv\widetilde{u}_0(L_X)$, $\widetilde{v}_{02}\equiv\widetilde{v}_0(L_X)$, $\widetilde{w}_2\equiv\widetilde{w}(L_X)$, $\partial\widetilde{w}_2/\partial x\equiv\partial\widetilde{w}/\partial x(L_X)$, (see Fig. 1(b) for the details of degree of freedom the element can support). Thus we can relate the nodal displacements and unknown coefficients as

$$\{\widetilde{\mathbf{u}}^{\mathbf{e}}\}=[\mathbf{B}]\{\mathbf{a}\} \tag{76}$$

From the forced boundary conditions, (Eqns. 59 to 61), nodal forces and unknown coefficients can be related as

$$\{\widetilde{\mathbf{F}}^{\mathbf{e}}\}=[\mathbf{C}]\{\mathbf{a}\} \tag{77}$$

where, $\{\widetilde{\mathbf{F}}^{\mathbf{e}}\}=\{\widetilde{N}_{x1}\ \widetilde{N}_{y1}\ \widetilde{V}_1\ \widetilde{M}_{y1}\ \widetilde{N}_{x2}\ \widetilde{N}_{y2}\ \widetilde{V}_2\ \widetilde{M}_{y2}\}$ and $\widetilde{N}_{x1}\equiv-\widetilde{N}_x(0)$, $\widetilde{N}_{y1}\equiv-\widetilde{N}_y(0)$, $\widetilde{V}_1\equiv-\widetilde{V}(0)$, $\widetilde{M}_{y1}\equiv-\widetilde{M}_y(0)$ and $\widetilde{N}_{x2}\equiv\widetilde{N}_x(L_X)$, $\widetilde{N}_{y2}\equiv\widetilde{N}_y(L_X)$, $\widetilde{V}_2\equiv\widetilde{V}(L_X)$, $\widetilde{M}_{y2}\equiv\widetilde{M}_y(L_X)$ (see Fig. 1(b)). From Eqns. 76 and 77 we can obtain a relation between transformed nodal forces and displacements similar to conventional FE

$$\{\widetilde{\mathbf{F}}^{\mathbf{e}}\}=[\mathbf{C}][\mathbf{B}]^{-1}\{\widetilde{\mathbf{u}}^{\mathbf{e}}\}=[\widetilde{\mathbf{K}}^{\mathbf{e}}]\{\widetilde{\mathbf{u}}^{\mathbf{e}}\} \tag{78}$$

where $[\widetilde{\mathbf{K}}^{\mathbf{e}}]$ is the exact elemental dynamic stiffness matrix. After the constants $\{\mathbf{a}\}$ are known from the above equations, they can substituted back to Eqn. 74 to obtain the transformed displacements $\widetilde{u}_0$, $\widetilde{v}_0$, $\widetilde{w}$, $\partial\widetilde{w}/\partial x$ at any given x.

6 Numerical Experiments

Here, the formulated 2-D WSFE is used to study axial and transverse wave propagation in an isotropic aluminum cantilever plate in both time and frequency domain. The plate shown in Fig. 2(a) is fixed at one edge

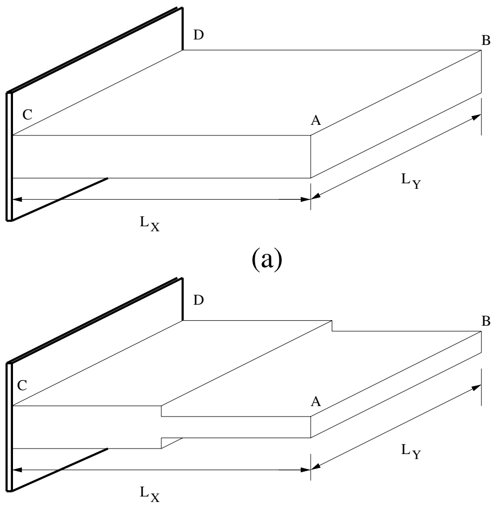

Figure 2 : Cantilever (a) uniform and (b) stepped plate.

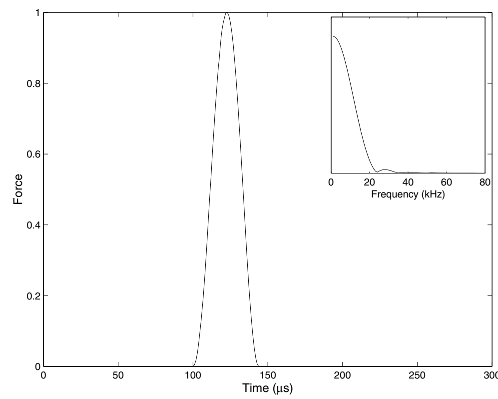

Figure 3 : Impulse load in time and frequency (inset) domain.

and free at the other edge along Y-axis. Numerical experiments are performed by considering the other two edges along X-axis to be free-free and fixed-fixed. The dimensions are L_X and L_Y along X and Y axis respectively, while the depth $(= 2h)$ is kept fixed at 0.01 m for the uniform plate shown in Fig. 2(a). However, both the lengths of the plate is kept small to show the effectiveness of the developed modeling technique in capturing the effects of these edges on the wave propagation behavior.

In all the examples provided, the load applied is an unit impulse of time duration 50 μs and frequency content 44 kHz. The load is shown in time and frequency domains in Fig. 3.

The load is applied at the free edge along the Y-axis and has a spatial distribution of $F(Y) = e^{-(Y/\alpha)^2}$, where, α is a constant and can be varied to change the Y-axis variation of the load.

The 2-D WSFE model is formulated with Daubechies scaling function of order $N = 22$ for temporal approximation and $N = 4$ for spatial approximation. The time sampling rate is $\triangle t = 2$ μs, unless otherwise mentioned, while the spatial sampling rate $\triangle Y$ is varied depending on L_Y and load distribution $F(y)$. As mentioned earlier, only one 2-D WSFE is used to simulate the responses of the uniform plate in Fig. 2(a). However, two elements are used to model the stepped plate in Fig. 2(b) because of the discontinuity present.

The accuracy of the responses simulated using the developed 2-D WSFE is validated with 2-D FE results. The FE meshing is done with 4-noded quadrilateral plane stress elements. Time integration is done using Newmark's scheme with time step 1 μs. The WSFE results are also compared with those obtained using FSFE to emphasize the advantages of the former method for wave propagation analysis of 2-D structures with finite dimension. Finally, the the developed technique is used in modeling further complex stepped plate shown in Fig. 2(b).

6.1 Axial wave propagation

The spectrum relation for the plate with $L_Y = 0.25$ m (see Fig. 2(a)) is plotted in Figs. 4 for axial wave propagation. The real and imaginary parts of the wavenumbers are plotted in Figs. 4(a) and (b) respectively for a Y wavenumber of 50 with $\triangle t = 8$ μs i.e for Nyquist frequency $f_{nyq} = 62.5$ kHz. Comparison is also made with FSFE [Chakraborty and Gopalakrishnan (2005)] results and it can be seen that WSFE predicts accurate wavenumbers, however, up to a certain fraction p_N of the Nyquist frequency f_{nyq}. Here, we see that wavenumber has significant real and imaginary parts. That is, the wave, as it propagates, also attenuates. Such waves are called inhomogeneous waves. As said earlier, this fraction p_N depends on the order of the Daubechies scaling function and is ≈ 0.6 for $N = 22$ [Mitra and Gopalakrishnan (2006)].

Figs. 5(a) and (b) show the axial velocities of a cantilever plate as in Fig. 2(a), measured at mid and quarter points respectively, on the free edge AB along the Y-axis. Here, the results simulated with the formulated 2-D WSFE is compared with 2-D FE results for validation.

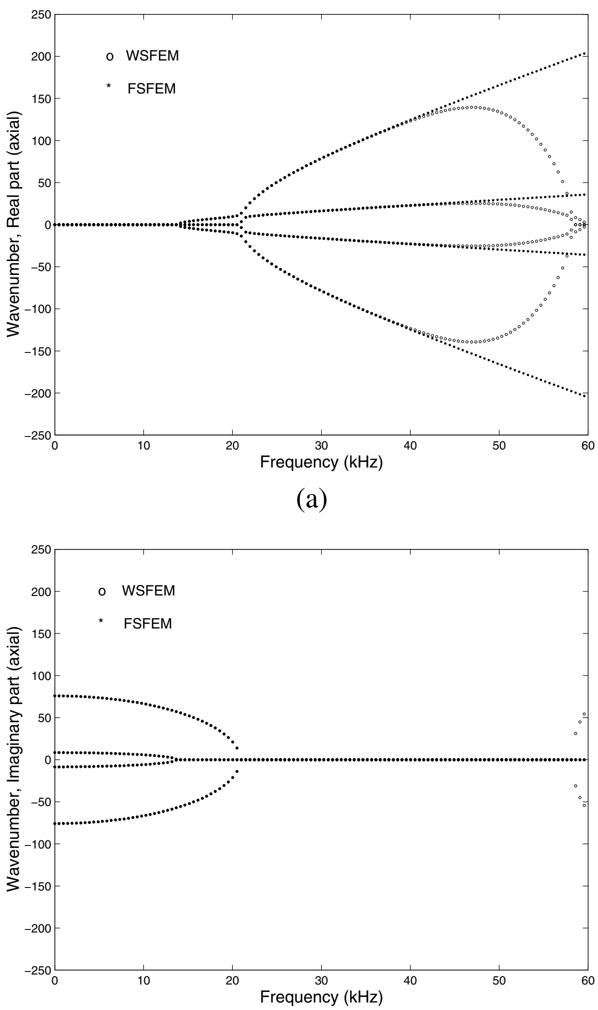

(a)

(b)

Figure 4 : The (a) real and (b) imaginary parts of the wavenumbers for axial wave propagation.

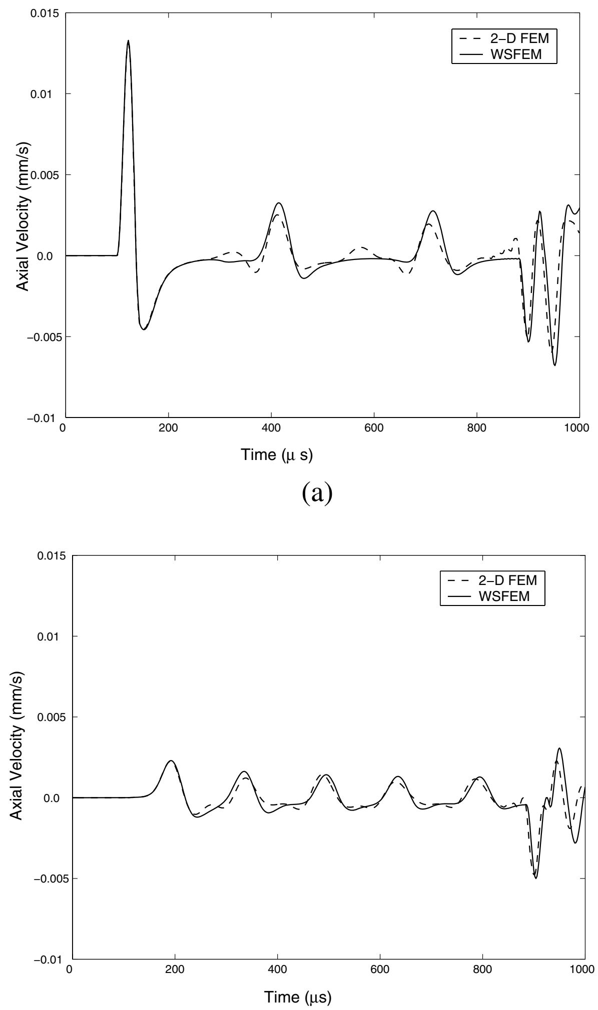

(a)

(b)

Figure 5 : Axial velocity of free-free cantilever plate (see Fig. 2(a)) with $L_X = 4.0$ m and $L_Y = 0.5$ m at measured at (a) mid and (b) quarter points of the free end AB.

It can be seen that the responses obtained with the two methods match very well. The plate has a finite dimension of $L_X = 4.0$ m and $L_Y = 0.5$ m and is free-free on the other two edges AC and BD along X-axis. L_Y is purposely chosen to be much smaller than L_X so as to show that the developed WSFE can efficiently capture the reflections from lateral edges AC and BD apart of those from the fixed edge CD. The impulse load (Fig. 3) with $\alpha = 0.05$ for Y-variation, is applied along the edge AB in axial direction. As mentioned earlier only one WSFE is used to model the structure and the time window is kept $T_w = 1024\ \mu s$ with number of sampling points $n = 512$ and $\triangle t = 2\ \mu s$. The number of discretization points along Y-axis is $m = 64$ and thus the spatial sampling rate is $\triangle Y = L_Y/(m-1) = 0.0079$ m. A very refined mesh with 12864 4-noded plane stress quadrilateral elements were used for the 2-D FE analysis, while, Newmark's scheme with time step 1 μs was used for time integration.

Similar comparison between WSFE and 2-D FE results is made in Fig. 6(a), but, here the two edges AC and BD are considered fixed. Otherwise the plate dimensions and loading conditions are same as the previous example. The axial velocities plotted are measured at mid-point of AB. Even for this case, the responses compare very well. It can be seen from the figure, that the first reflection from fixed edges AC and BD is reversed if compared with the similar response of the free-free plate shown in Fig. 5(a).

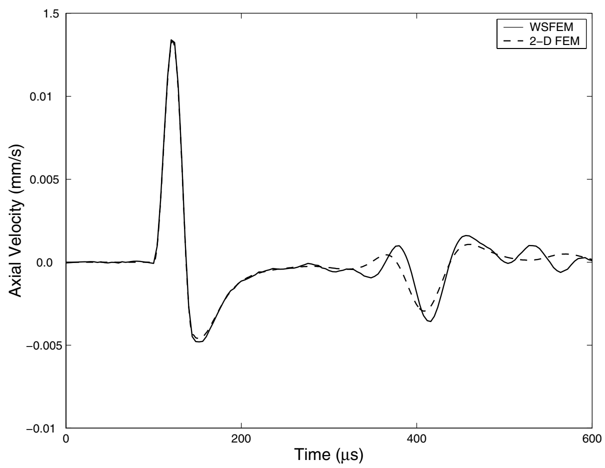

(a)

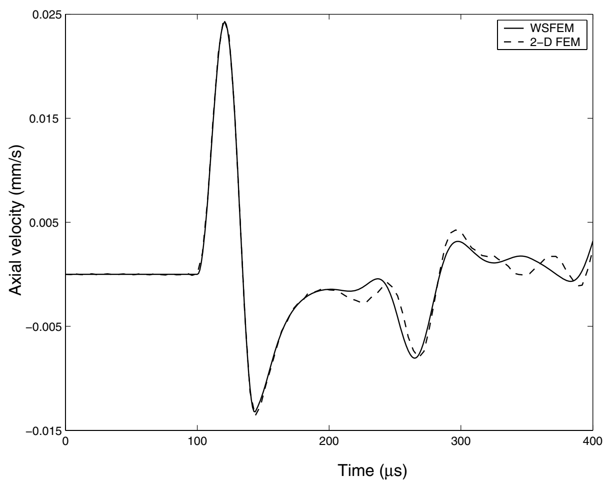

(b)

Figure 6 : Axial velocity of fixed-fixed cantilever plate (see Fig. 2(a)) with $L_X = 4.0$ m, (a) $L_Y = 0.5$ m and (b) $L_Y = 0.25$ m measured at mid-point of free end AB.

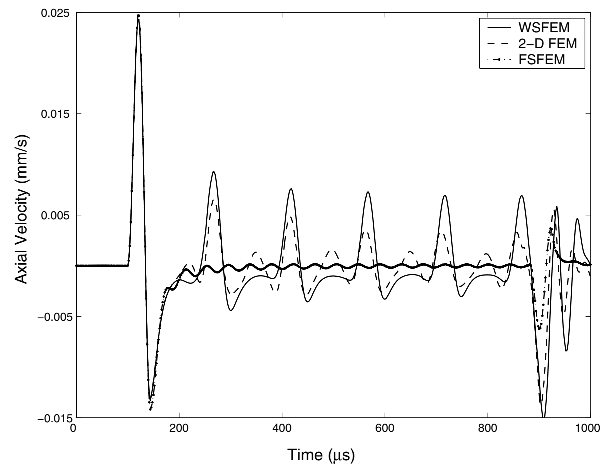

(a)

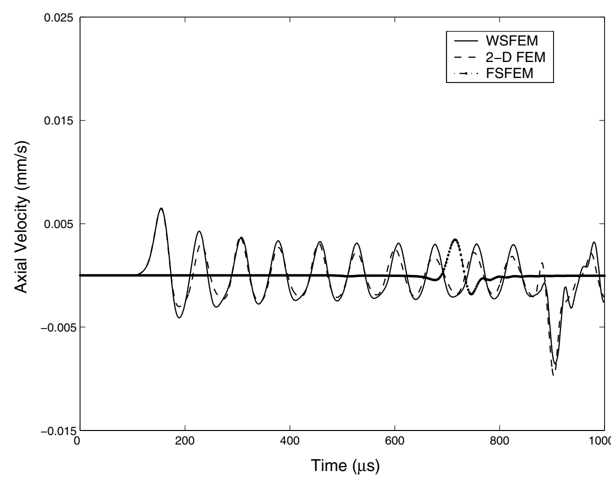

(b)

Figure 7 : Axial velocity of free-free cantilever plate (see Fig. 2(a)) with $L_X = 4.0$ m and $L_Y = 0.25$ m at measured at (a) mid and (b) quarter points of the free end AB.

In Fig. 6(b), the axial velocity at the mid-point of AB simulated with a single WSFE is plotted and shows good comparison with 2-D FE results for a plate very similar to that in last example, except, $L_Y = 0.25$ m. The unit impulse load is applied along AB in axial direction, however, here $\alpha = 0.03$ for Y-variation. The FE mesh, time integration scheme and the parameters involved in WSFE modeling is similar to the previous case.

The axial velocities at the mid and quarter points of edge AB (see Fig. 2(a)) are plotted in Figs. 7(a) and (b) respectively. The plate is free along the edges AC and BD, the dimensions are $L_X = 4.0$ m and $L_Y = 0.25$ m. The same impulse load with $\alpha = 0.03$ is applied along AB in axial direction. The results are validated with 2-D FE analysis. The details of WSFE and FE modeling are as in previous example. The main aim of the example is to provide a comparison of the WSFE results with those obtained using FSFE. As stated earlier, it can be seen from the figures, that unlike WSFE, FSFE is unable to accurately capture the reflections from the lateral edges, AC and BD in this example. Thus, for structures with finite or short dimensions, FSFE results will deviate substantially from the actual responses. In addition, simulation with FSFE requires "throw-off" element to impart artificial damping to the structure and a large time window

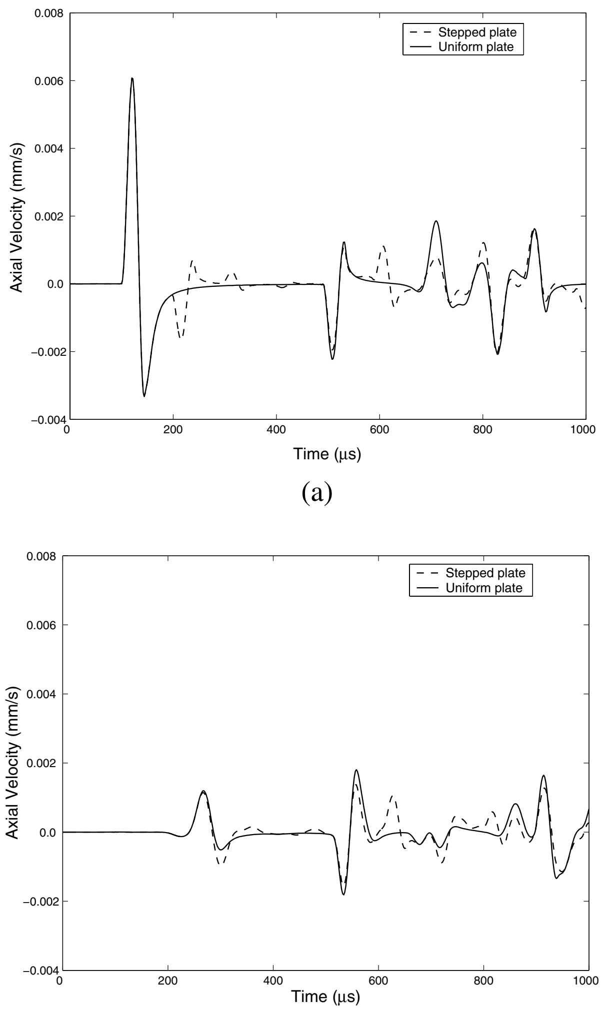

(a) (b)

Figure 8 : Axial velocity (mm/s) of free-free uniform and stepped cantilever plate (see Fig. 2(a) and (b)) with $L_X = 2.0$ m and $L_Y = 1.0$ m at (a) mid and (b) quarter points on edge AB.

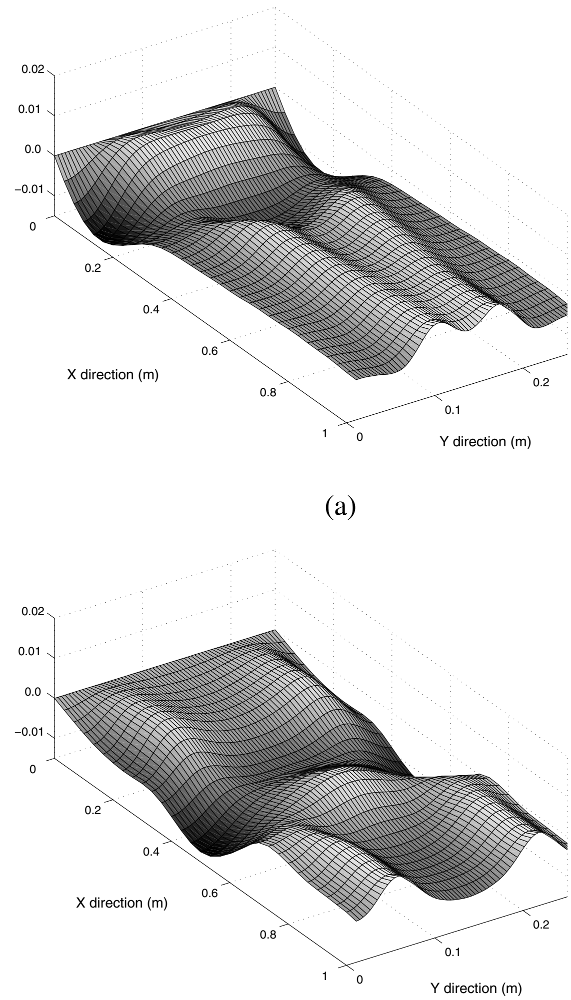

(a) (b)

Figure 9 : Axial velocity (mm/s) of free-free cantilever plate (see Fig. 2(a)) with $L_X = 1.0$ m and $L_Y = 0.25$ m at time instances (a) $T = 248\ \mu s$ and (b) $T = 372\ \mu s$.

$T_w = 16384\ \mu s$ ($\triangle t = 2\ \mu s$ and $n = 8192$) to remove the distortions due to "wrap around" problem. It should be restated here, that the accuracy of the response simulated using WSFE is independent of the time window T_w which is chosen as required for observation.

In Figs. 8(a) and (b), the axial velocities at the mid and quarter points on the edge AB are plotted respectively for both uniform and stepped plates shown in Figs. 2(a) and (b). The plates have free-free lateral edges AC, BD and $L_X = 2.0$ m, $L_Y = 1.0$ m. The uniform plate has a depth of $h = 0.01$ m as used in earlier examples. In the stepped plate, the depth of thicker part of length $L_{X1} = 1.5$ m is $h = 0.02$ m and is $h = 0.01$ m for the thinner part of length $L_{X2} = 0.5$ m. The responses measured are for impulse load with $\alpha = 0.03$ applied along the free edge AB. As mentioned earlier, modeling of the stepped plate requires two WSFE due to the discontinuity present. However, the uniform plate is modeled with a single WSFE and number of sampling points in Y direction are $m = 128$ for both the cases. It can be seen from the Figs. 8(a) and (b), that though the velocities do not differ much in amplitude, the responses of the stepped plate show more reflections arising from the discontinuity present. For example, in Fig. 8(a), the response of the stepped plate shows an additional wave immediately after the incident wave and it

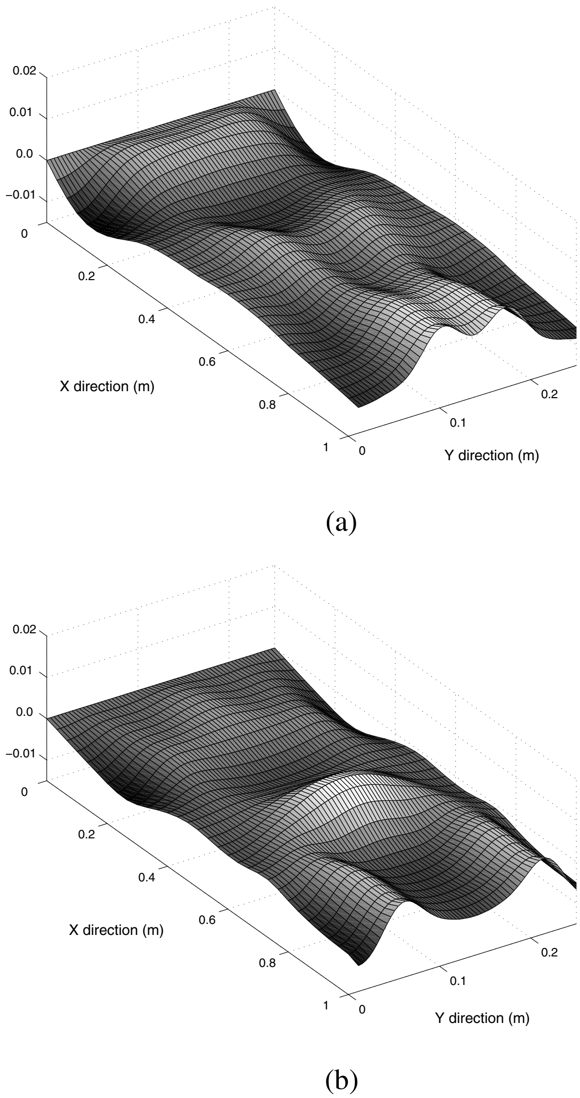

Figure 10 : Axial velocity (mm/s) of stepped free-free cantilever plate (see Fig. 2(b)) with $L_X = 1.0$ m and $L_Y = 0.25$ m at time instances (a) $T = 248$ μs and (b) $T = 372$ μs.

is due to the reflection from the discontinuity present at a distance $L_{X2} = 0.5$ m from AB or location of incidence.

Figs. 9(a) and (b) show the snapshots of axial velocities of the cantilever plate with free-free lateral edges (AC and BD) shown in Fig. 2(a) at time instances $T = 248$ μs and $T = 372$ μs respectively. The plate dimensions are $L_X = 1.0$ m and $L_Y = 0.25$ m, and is modeled using single WSFE with $m = 64$ sampling points on Y-direction. The loading condition is same as in previous example. However, here shorter dimensions are chosen to study the effects of the reflections from all boundaries which include the two free lateral edges (AC and BD) and the other two fixed free ends (CD and AB). It should be mentioned here that the velocities at all the sampling points along Y direction and at any points along X direction used to obtain the snapshots are obtained from a single simulation. In Figs. 10(a) and (b), similar axial velocities snapshots under the same loading condition are presented for time instances $T = 248$ μs and $T = 372$ μs respectively. However, here, the plate has a stepped form as shown in Fig. 2(b), with $L_X = 1.0$ m and $L_Y = 0.25$ m, while the depth is $h = 0.02$ m for the thicker half and $h = 0.01$ m for the remaining half of the plate. Due to the discontinuities present, two WSFE is assembled to model the plate and the number of sampling points in Y-direction is $m = 64$. It can be seen from the snapshots that there is much difference in the deformation patterns rather than the amplitudes of the axial responses of uniform and stepped plates. This is as expected, because similar to that observed in the previous example, the response of the stepped plate will contain reflections arising from the discontinuity apart from the boundaries.

6.2 Transverse wave propagation

Similar numerical experiments and validations as performed for axial wave propagation are also done for transverse wave propagation due to out-of-plane loading. First, in Figs. 11(a) and (b), the real and imaginary parts of the wavenumbers for transverse wave propagation are shown respectively. The wavenumbers are plotted up to the Nyquist frequency $f_{nyq} = 62.5$ kHz for time sampling rate $\triangle t = 8$ μs and the Y-wavenumber considered is 100. From the figures, we see that waves are inhomogeneous in nature. As in the previous case of axial wave propagation, the wavenumbers obtained from both FSFE and WSFE are presented and can be seen that WSFE gives accurate prediction up to the allowable frequency range i.e the fraction p_N of f_{nyq}.

The transverse velocities at mid and quarter points on the free edge AB of the cantilever plate shown in Fig. 2(a) are presented in Figs. 12(a) and (b) respectively. The responses obtained using the present 2-D WSFE method is compared with 2-D FE results and a good match is observed. The two edges AC and BD of the plate are free and the dimensions are given as $L_X = 4.0$ m and $L_Y = 0.5$ m. The unit impulse load is applied along the free edge AB in transverse direction and the Y-distribution is obtained using $\alpha = 0.05$. Single WSFE is used to simu-

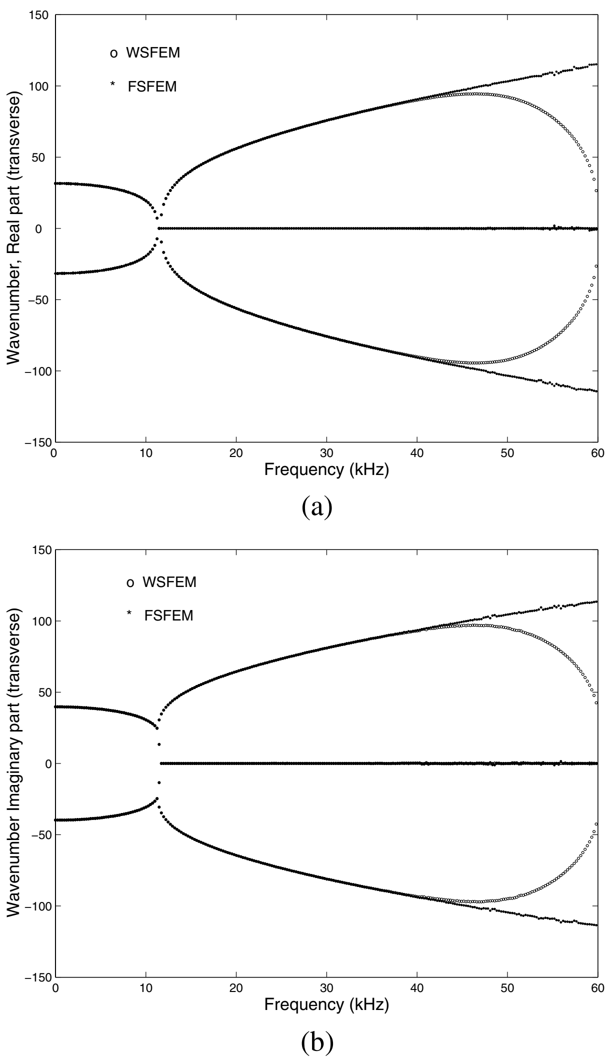

Figure 11 : The (a) real and (b) imaginary parts of the wavenumbers for transverse wave propagation.

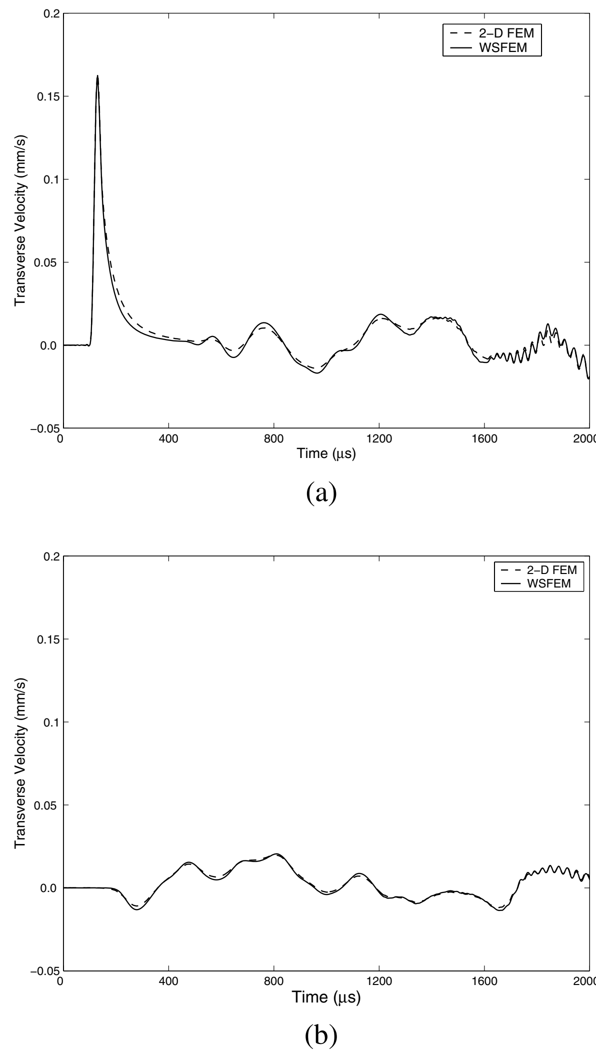

Figure 12 : Transverse velocity of free-free cantilever plate (see Fig. 2(a)) with $L_X = 4.0$ m and $L_Y = 0.5$ m at measured at (a) mid and (b) quarter points of the free end AB.

late the responses with $n = 1024$, $\triangle t = 2\ \mu s$ and thus $T_w = 2048\ \mu s$. The spatial sampling rate is $\triangle Y = 0.0079$ m, number of sampling points being $m = 64$. The FE mesh has 12864, 4-noded plane stress quadrilateral elements and time integration is done using Newmark's scheme with time step 1 μs.

In Figs. 13(a) and (b), the transverse velocities are plotted for the mid and quarter points of the free edge AB respectively. The plate configuration is same as the previous example except $L_Y = 0.25$ m. As before the unit impulse load with $\alpha = 0.03$ is applied along AB in transverse direction. In these figures, the responses simulated using WSFE, 2-D FE and FSFE methods are plotted for comparison. The parameters for WSFE modeling, FE mesh and Newmark's time integration are similar to those in the last example. It can be seen that the WSFE and 2-D FE results correlate very well. Similar to axial wave propagation, FSFE cannot capture the effect of the lateral edges AC and BD even for transverse wave propagation. In addition, for structures with finite/short dimensions as in this example, the FSFE results varies considerably from the 2-D FE results. As mentioned earlier, apart from the above limitation, simulation with FSFE requires the semi-infinite "throw-off" element to add damping to the structure and a large time window $T_w = 16384\ \mu s$ i.e number of sampling points $n = 8192$ with $\triangle t = 2\ \mu s$

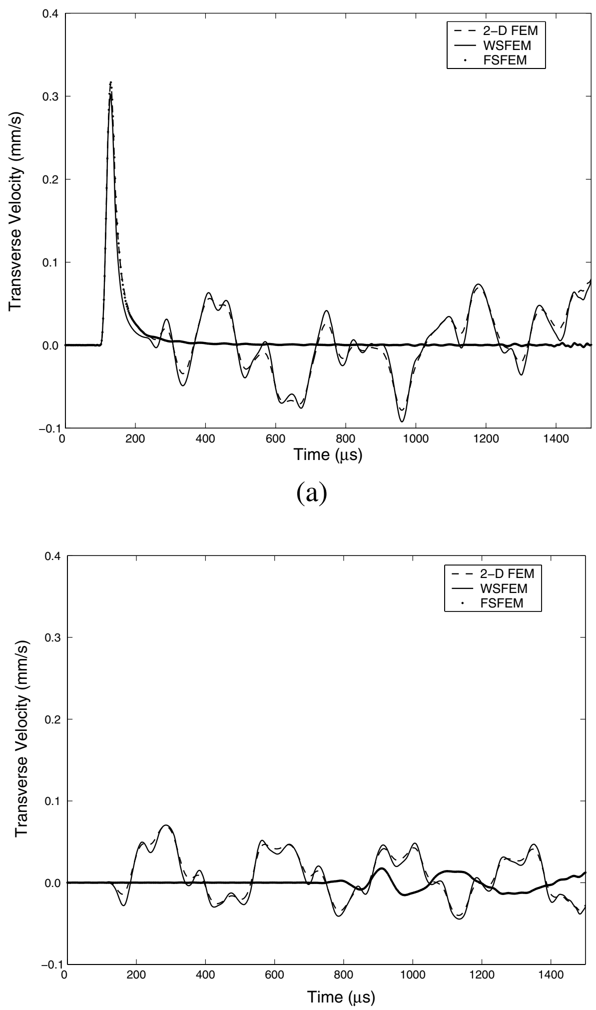

Figure 13 : Axial velocity of free-free cantilever plate (see Fig. 2(a)) with $L_X = 4.0$ m and $L_Y = 0.25$ m at measured at (a) mid and (b) quarter points of the free end AB.

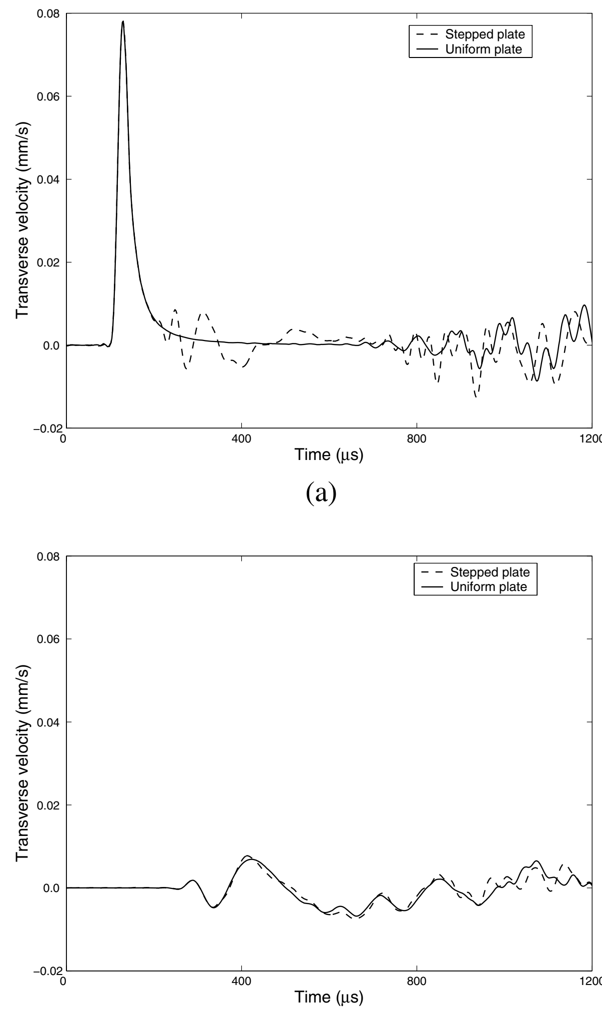

Figure 14 : Transverse velocity (mm/s) of free-free uniform and stepped cantilever plate (see Fig. 2(a) and (b)) with $L_X = 2.0$ m and $L_Y = 1.0$ m at (a) mid and (b) quarter points of free edge AB.

to remove the distortions resulting from "wrap around". However, it can be seen from this example that the developed WSFE is free from any of the above problems, also for transverse wave propagation.

In Figs. 14(a) and (b), the transverse velocities at the mid and quarter points on the edge AB are plotted respectively for both uniform and stepped plates shown in Figs. 2(a) and (b). The plates have free-free lateral edges AC, BD and $L_X = 2.0$ m, $L_Y = 1.0$ m. The uniform plate has a depth of $h = 0.01$ m as used in earlier examples. In the stepped plate, the depth of thicker part of length $L_{X1} = 1.75$ m is $h = 0.02$ m and is $h = 0.01$ m for the thinner part of length $L_{X2} = 0.25$ m. The responses measured are for impulse load with $\alpha = 0.03$ applied along the free edge AB. Due to the discontinuity present, two WSFE are used to model the stepped plate. However, the uniform plate is modeled with a single WSFE and number of sampling points in Y direction are $m = 128$ for both the cases. From Figs. 14(a) and (b) it can be seen that though the velocities do not differ much in amplitude, the response of the stepped plate differ considerably from that of the uniform plate because of the reflections arising from the discontinuity present. In Fig. 14(a), the response of the stepped plate shows an additional

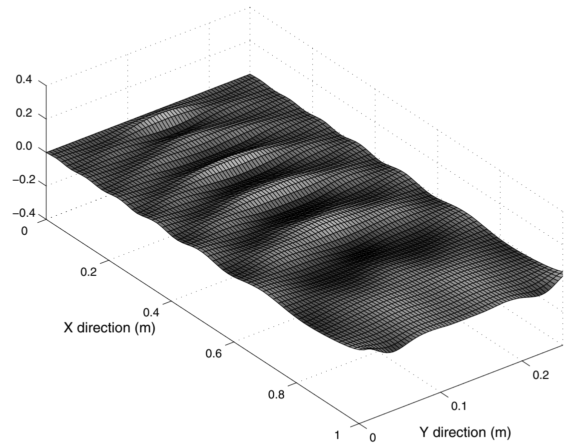

(a)

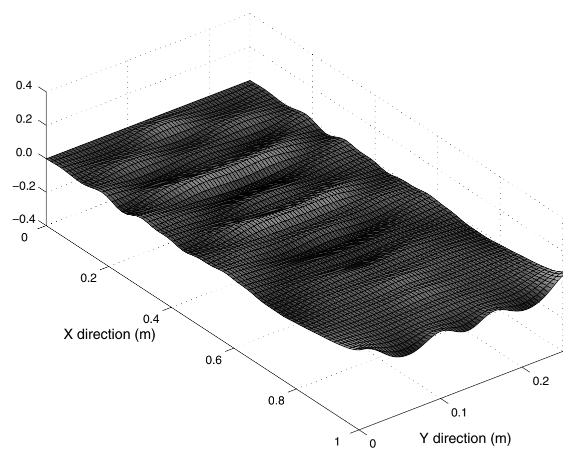

(b)

Figure 15 : Transverse velocity (mm/s) of free-free cantilever plate (see Fig. 2(a)) with $L_X = 1.0$ m and $L_Y = 0.25$ m at time instances (a) $T = 372$ μs and (b) $T = 500$ μs.

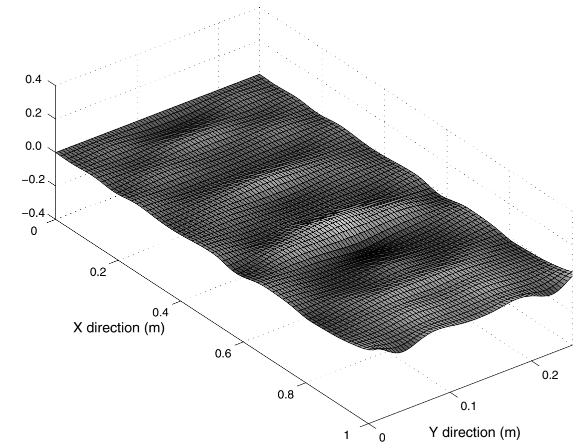

(a)

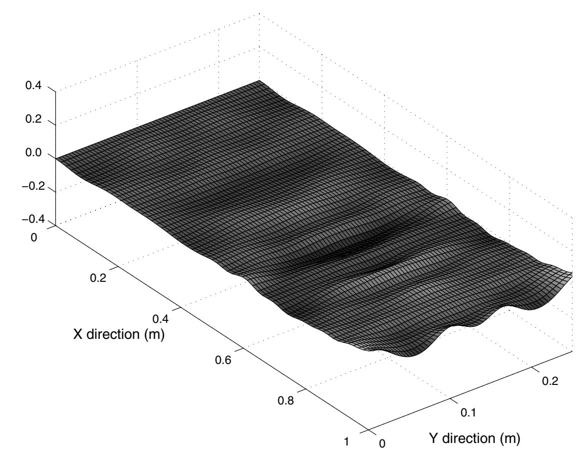

(b)

Figure 16 : Transverse velocity (mm/s) of stepped free-free cantilever plate (see Fig. 2(b)) with $L_X = 1.0$ m and $L_Y = 0.25$ m at time instances (a) $T = 372$ μs and (b) $T = 500$ μs.

wave after the incident wave and it is the wave reflected from the discontinuity present at a distance $L_{X2} = 0.25$ m from AB. The responses of the plates at the quarter point shown in Fig. 14(b) do not vary much since here, within the time window observed the reflections from the lateral edges are predominant. However, the responses will start deviating at a later time.

Figs. 15(a) and (b) show the snapshots of the transverse velocities of the cantilever plate with free lateral edges AC and BD shown in Fig. 2(a), at time instances $T = 372$ μs and 500 μs respectively. The plate dimensions are $L_X = 1.0$ m and $L_Y = 0.25$ m, and is modeled using single WSFE with $m = 64$ sampling points in Y direction. The impulse load with $\alpha = 0.03$ is applied at the free edge AB. Similar to the snapshots of axial velocities, here also the velocities at all the sampling points along Y direction and at any points along X directions are available by performing only one simulation. In Figs. 16(a) and (b), similar snapshots of transverse velocities under the same loading conditions are presented for time instances $T = 372$ μs and 500 μs respectively. However, here, the plate has a stepped form as shown in Fig. 2(b), with $L_X = 1.0$ m and $L_Y = 0.25$ m, the thickness are $h = 0.01$ m for the half near free edge AB and $h = 0.02$ m for the other half of the plate near the fixed end. Similar to the previous example, two WSFE are used to model the plate due to discontinuity present and the number of sampling points along Y direction is $m = 64$. It can be observed from the Figs. 15 and 16, that the small dimensions of the plates result in multiple reflections from all the edges and are captured with the snapshots. Further, it can be seen that, the distribution of the transverse velocity for the stepped plate varies considerably from that of the uniform plate. This is primarily due to the presence of the discontinuity in the stepped plate which results in reflections in addition to those from the four edges.

7 Conclusions

In this paper, a 2-D wavelet based spectral method is developed for wave propagation studies. Spectral element method proves to be an efficient alternative FE analysis of wave propagation problems and decreases computational costs substantially. The formulated spectral finite element technique circumvents several important limitations of the conventional FFT based spectral finite element method, while retaining the advantages like computational efficiency, simultaneous time and frequency domain analysis. Firstly, the localized nature of the Daubechies basis functions for WSFE method allows modeling of plate structures with finite dimensions which is otherwise not possible with the corresponding FFT based method. In addition, similar to 1-D WSFE, the 2-D WSFE is also free from “wrap around” problem associated with FSFE due to the assumption of periodicity in time approximation. Consequence of this is that FSFE, unlike WSFE, cannot model undamped finite length structures and even in presence of damping, larger time window is needed to remove the distortions arising from “wrap around”.

First, the responses simulated using 2-D WSFE are validated with 2-D FE results for both axial and transverse wave propagation. Numerical experiments are also performed to emphasize the advantages of WSFE over FSFE. Finally, wave propagation in a stepped plate is studied to show effectiveness of the developed technique in modeling relatively complex structures.

References

Andreaus, U.; Batra, R. C.; Porfiri, M. (2005): Vibrations of Cracked Euler-Bernoulli Beams using Meshless Local Petrov-Galerkin (MLPG) Method. *CMES: Computer Modeling in Engineering and Sciences*, vol. 9, pp. 111–132.

Beylkin, G. (1992): On the representation of operators in bases of compactly supported wavelets. *SIAM Journal of Numerical Analysis*, vol. 6, pp. 1716–1740.

Chakraborty, A.; Gopalakrishnan, S. (2004): A higher order spectral element for wave propagation analysis in functionally graded materials. *Acta Mechanica*, vol. 172, pp. 17–43.

Chakraborty, A.; Gopalakrishnan, S. (2004): A spectrally formulated finite element for wave propagation analysis in layered composite media. *International Journal of Solids and Structures*, vol. 41, pp. 5155–5183.

Chakraborty, A.; Gopalakrishnan, S. (2004): Wave propagation in inhomogeneous layered media: Solution of forward and inverse problems. *Acta Mechanica*, vol. 169, pp. 153–185.

Chakraborty, A.; Gopalakrishnan, S. (2005): A spectrally formulated plate element for wave propagation analysis in anisotropic material. *Computer Methods in Applied Mechanics and Engineering*, vol. 194, pp. 4425–4446.

Chen, M. Q.; Hwang, C.; Shih, Y. P. (1996): The computation of wavelet-Galerkin approximation on a bounded interval. *International Journal for Numerical Methods in Engineering*, vol. 39, pp. 2921–2944.

Daubechis, I. (1992): *Ten lectures on wavelets.* CBMS-NSF Series in Applied Mathematics (SIAM, Philadelphia).

Davis, P. J. (1963): *Interpolation and Approximation.* Blaisdell, New York.

Doyle, J. F. (1999): *Wave Propagation in Structures.* Springer, New York.

Han, X.; Ding, H.; Liu, G. R. (2005): Elastic waves in a hybrid multilayered piezoelectric plate. *CMES: Computer Modeling in Engineering and Sciences*, vol. 9, pp. 49–56.

Mitra, M.; Gopalakrishnan, S. (2005): Spectrally Formulated Wavelet Finite Element for Wave Propagation and Impact Force Identification in Connected 1-D

Waveguides. *International Journal of Solids and Structures*, vol. 42, pp. 4695–4721.

Mitra, M.; Gopalakrishnan, S. (2006): Extraction of wave charateristics from wavelet based spectral finite element formulation. *Mechanical Systems and Signal Processing. (In Press).*

Nayfeh, A. H.; Pai, P. F. (2004): *Linear and Nonlinear Structural Analysis.* Wiley, New Jersey.

Patton, R. D.; Marks, P. C. (1996): One dimensional finite elements based on the Daubechies family of wavelets. *AIAA Journal*, vol. 34, pp. 1696–1698.

Qian, Z.; Han, Z.; Ufimtsev, P.; Atluri, S. (2004): Non-Hyper-Singular Boundary Integral Equations for Acoustic Problems, Implemented by the Collocation-Based Boundary Element Method. *CMES: Computer Modeling in Engineering and Sciences*, vol. 6, pp. 133–144.

Rizzi, S. A. (1989): *A spectral analysis approach to wave propagation in layered solids.* PhD dissertation, Purdue University.

Rizzi, S. A.; Doyle, J. F. (1989): Force identification for impact problem on a half plane. *Computational Techniques for Contact, Impact, Penetration and Perforation of Solids*, vol. 103, pp. 163–182.

Rizzi, S. A.; Doyle, J. F. (1991): Force identification for impact of a layered system. *Computational Aspects of Contact, Impact and Penetration, Elmepress International*, pp. 222–241.

Solie, L.; Auld, B. (1973): Elastic waves in free anisotrpic plates. *Journal of Acoustical Society of America*, vol. 54, pp. 50–65.

Williams, J. R.; Amaratunga, K. (1994): Introduction to wavelets in engineering. *International Journal for Numerical Methods in Engineering*, vol. 37, pp. 2365–2388.

Williams, J. R.; Amaratunga, K. (1997): A Discrete wavelet transform without edge effects using wavelet extrapolation. *Journal of Fourier Analysis and Applications*, vol. 3, pp. 435–449.